Development of a Polarimetric 50-GHz Spectrometer for Temperature Sounding in the Middle Atmosphere

Witali Krochin , Gunter Stober, and Axel Murk

Abstract—This article addresses the further development of the ground-based temperature radiometer TEMPERA, which measures atmospheric microwave radiation in one linear polarization in order to retrieve temperature profiles up to an altitude of 50 km (Stähli *et al.*, 2013). The latest innovation is a new polarimetric receiver, which allows observing the atmosphere simultaneously in left- and right-circular polarization. In combination with an adapted inversion method, the fully polarimetric analysis can improve the accuracy and extends the vertical upper limit of retrieved temperature profiles. Comparisons between single polarization and fully polarimetric retrievals with simulated atmospheric spectra are presented, and the influence of the Earth's magnetic field is analyzed. In addition, we propose a simple calibration method for fully polarimetric radiometers and present first atmospheric spectra measured with the new TEMPERA-C instrument.

Index Terms—Geomagnetism, microwave antennas, microwave radiometry, passive microwave remote sensing, radiometers, radiometry, remote sensing.

I. INTRODUCTION

ATMOSPHERIC temperature observations at the stratosphere and lower mesosphere are crucial for numerical weather prediction and to understand the climatological behavior from the surface up to space. Tropospheric temperature profiles are derived routinely by remote sensing with spaceborne and ground-based microwave radiometers observing the wing of the oxygen absorption line complex in the 50–60-GHz band. The standard instruments for ground-based tropospheric temperature sounding use typically up to 15 channels with a frequency resolution between 10 MHz and 2 GHz [2]. Spaceborne instruments can have even more channels and a higher resolution [3], [4]. The addition of a high-resolution spectrometer allows us to resolve also several narrow line features, which can be used to retrieve temperature profiles in the middle atmosphere [1], [5]. Measurements in this altitude region between 12 and 80 km are important to understand the global atmospheric dynamics, such as planetary waves, atmospheric tides, and gravity waves, and dynamical induced processes such as sudden stratospheric warmings [6], [7]. In particular, atmospheric tides have become a vital science topic. These atmospheric waves cause periodic

oscillations in temperature, which propagate/migrate over the whole globe and are present from the stratosphere up to the mesosphere and even the thermosphere. These waves carry energy and momentum from their source region to the altitude of their dissipation and, thus, are essential for the energetic coupling between the different vertical atmospheric layers.

Recently, an inversion algorithm for a ground-based single-polarization TEMPErature RAdiometer (TEMPERA) [1] was revised and extended to account for the Zeeman splitting (see Section IV) in the forward model [8]. This upgrade improved the upper altitude limit for temperature profile retrievals from single polarized spectra from 48 to 53 km. Furthermore, it was also demonstrated that temperatures at higher altitudes cannot be retrieved with single polarization due to the Zeeman effect in the line center resulting in an additional line broadening posing a natural limit for the former instrument.

In this article, it is demonstrated that the polarimetric decomposition of the atmospheric emission spectra provides a possibility to further enhance the altitude coverage to around 60 km and to study features of the Earth's magnetic field.

This article addresses the development of a fully polarimetric ground-based temperature radiometer, called TEMPERA-C. Based on simulated data, we compare the retrieval capabilities of a fully polarimetric instrument with one that observes only single linear polarization. In addition, we present first sensitivity investigations to analyze the magnetic field features. The last sections provide a description of the TEMPERA-C receiver and the first polarimetric observations of atmospheric emission lines.

II. RETRIEVAL OF TEMPERATURE PROFILES

The method to retrieve atmospheric temperature profiles presented in this article is based on a numerical inversion of atmospheric microwave spectra with Atmospheric Radiative Transfer Simulator (ARTS) [9]. Atmospheric oxygen emits microwave radiation through rotational transitions. The shape of these emission lines is determined by pressure broadening. Fig. 1 shows a typical brightness temperature spectrum simulated with the ARTS. The red box highlights the frequency band covered by the high-resolution spectrometer of TEMPERA. The temperature profile in the stratosphere is retrieved from the pressure broadened lineshape of the two emission lines included in this spectral region. The mathematical formalism of the ARTS follows the optimal estimation method from Rodgers [10]. The measured spectrum **y** results from the atmospheric state **x** and the forward
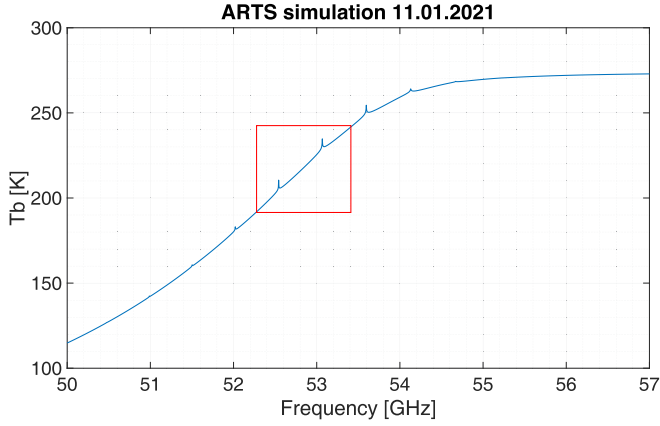
Fig. 1. Brightness temperature spectrum simulated for an elevation angle of $60°$. The red box highlights the two stratospheric emission lines, which are observed with TEMPERA.

model F

$$\mathbf{y} = F(\mathbf{x}) + \boldsymbol{\epsilon} \tag{1}$$

where $\boldsymbol{\epsilon}$ is the measurement error. The challenge is to retrieve $\mathbf{x}$ from the measurement $\mathbf{y}$. In our case, the inversion of the measured spectra into a vertical temperature profile leads to an inversion problem that is ill-posed. One of the reasons is that there are an infinite amount of solutions $\mathbf{x}$ for a given measurement $\mathbf{y}$. The optimal state $\tilde{\mathbf{x}}$ is the state that maximizes the probability $P(\mathbf{x}|\mathbf{y})$ for a given measurement $\mathbf{y}$. Using Bayes' theorem with the assumption that $\mathbf{x}$ and $\mathbf{y}$ have Gaussian probability density distributions, the optimization problem can be transformed into the problem of minimizing the cost function

$$J(\mathbf{x}) = -2\ln P(\mathbf{x}|\mathbf{y}) = [\mathbf{y} - F(\mathbf{x})]^T \mathbf{S}_\epsilon^{-1} [\mathbf{y} - F(\mathbf{x})]$$
$$+ [\mathbf{x} - \mathbf{x}_a]^T \mathbf{S_a} [\mathbf{x} - \mathbf{x}_a]. \tag{2}$$

Here, S_ϵ is the measurement error covariance matrix, $\mathbf{x}_a$ is the preknowledge background state of the atmosphere (apriori state), and $\mathbf{S}_a$ is its covariance matrix. The resulting matrix equation is solved by a Levenberg–Marquardt algorithm. Writing the optimal state as $\tilde{\mathbf{x}} = R(\mathbf{y}, \mathbf{x}_a)$, the averaging kernel matrix (AVK) is defined as

$$\mathbf{A} = \frac{\partial R}{\partial \mathbf{y}} \frac{\partial F}{\partial \mathbf{x}} = \mathbf{G}_y \mathbf{K}_x \tag{3}$$

that is basically the Jacobian matrix of the forward model $\mathbf{K}_x = \partial F/\partial \mathbf{x}$ weighted with the gain matrix $\mathbf{G}_y = \partial R/\partial \mathbf{y}$. The half-width of the rows of $\mathbf{A}$ can be regarded as a measure of the effective vertical resolution of the retrieval. The AVK is widely used to illustrate the performance of a retrieval. Another important quality control parameter is the measurement response vector (MR) defined as

$$\mathbf{MR}_i = \frac{\mathbf{A}_i \mathbf{x}_a}{\mathbf{x}_{ai}} \tag{4}$$

where $\mathbf{A}_i$ is the ith row of the AVK matrix and $\mathbf{x}_{ai}$ is the ith entry of the apriori vector. For an ideal retrieval, the entries $\mathbf{MR}_i$

are equal to 1, while values below 0.6 indicate that the retrieved state depends mostly on the apriori state.

A more detailed discussion of the retrieval algorithm can be found in [8] and is not repeated here. The only difference in the retrievals presented in this article is that simulated emission lines were used instead of observed emission lines and that the retrieval was performed with two left-circular-polarized (LCP)/right-circular-polarized (RCP) spectra instead of one linearly polarized spectrum.

III. STOKES PARAMETERS

To describe the polarization states, we use the concept of Stokes parameters defined in the following way [11]. A monochromatic plane wave propagating in the z-direction in complex notation has the form

$$\mathbf{E}(t) = \mathbf{E}(0)e^{j(\omega t - \mathbf{kz} - \phi)}. \tag{5}$$

The directions orthogonal to the z-axis are denoted as h and v. The position of the receiver can be set to zero $z = 0$ so that the h and v components have the form

$$E_h(t) = E_h(0)e^{j(\omega t - \phi_h)} \tag{6}$$

$$E_v(t) = E_v(0)e^{j(\omega t - \phi_v)}. \tag{7}$$

The Stokes parameters for linear polarized field components are

$$I = |\langle E_h \rangle|^2 + |\langle E_v \rangle|^2 \tag{8}$$

$$Q = |\langle E_h \rangle|^2 - |\langle E_v \rangle|^2 \tag{9}$$

$$U = 2\Re\left(\langle E_h E_v^* \rangle\right) \tag{10}$$

$$V = 2\Im\left(\langle E_h E_v^* \rangle\right). \tag{11}$$

The brackets $\langle\rangle$ denotes the expectation value over a time period $\Delta t \gg {}^{2\pi}/\omega$, E_α^* denotes the complex conjugation, $\Re$ is the real part, and $\Im$ is the imaginary part. We have ignored the prefactors in these equations, because these terms are determined after a total power calibration. To derive the LCP and RCP field components, the first and fourth Stokes parameters expressed with circular polarized fields will be used

$$I = |\langle E_{\text{LCP}} \rangle|^2 + |\langle E_{\text{RCP}} \rangle|^2 \tag{12}$$

$$V = |\langle E_{\text{LCP}} \rangle|^2 - |\langle E_{\text{RCP}} \rangle|^2. \tag{13}$$

IV. ALTITUDE LIMITATION: ZEEMAN EFFECT

The observed emission lines are originated from rotational transitions of the oxygen molecule. The interaction with the Earth's magnetic field splits rotational energy levels into several sublevels. Therefore, one emission line splits into different lines, depending on the orientation of the angular momentum, magnetic moment, magnetic field, and polarization. For emission lines measured with a linearly polarized radiometer, this results in a broadening of the line center, which also depends on the orientation between the magnetic field lines and the line of sight of the instrument [12], [13].

Fig. 2 compares a measured emission line of the TEMPERA instrument with ARTS simulations. The simulations were performed with and without the Zeeman effect for the same linear
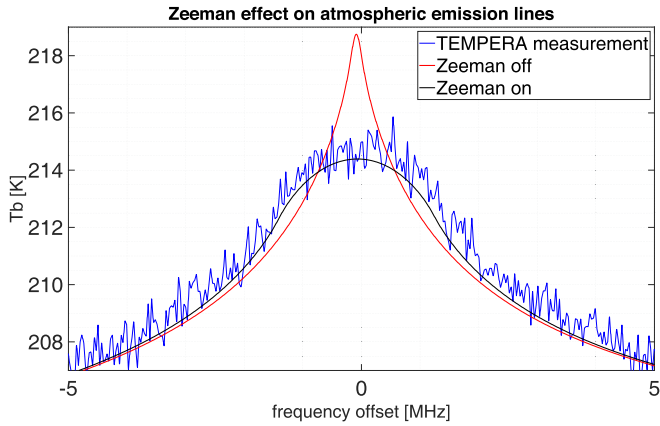
Fig. 2. Measurement with TEMPERA on the January 1, 2022 in Bern, and ARTS simulations with and without Zeeman effect. The line center is at 53.067 GHz.
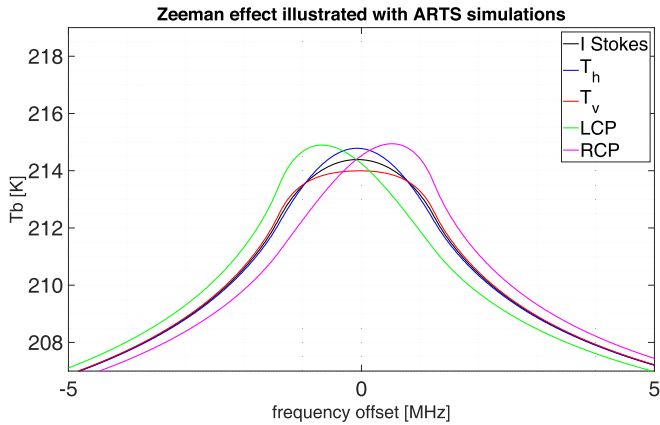

Fig. 3. Simulated line centers for vertical, horizontal, and left- and right-circular-polarized radiation in comparison to the total intensity. The line center is at 53.067 GHz.
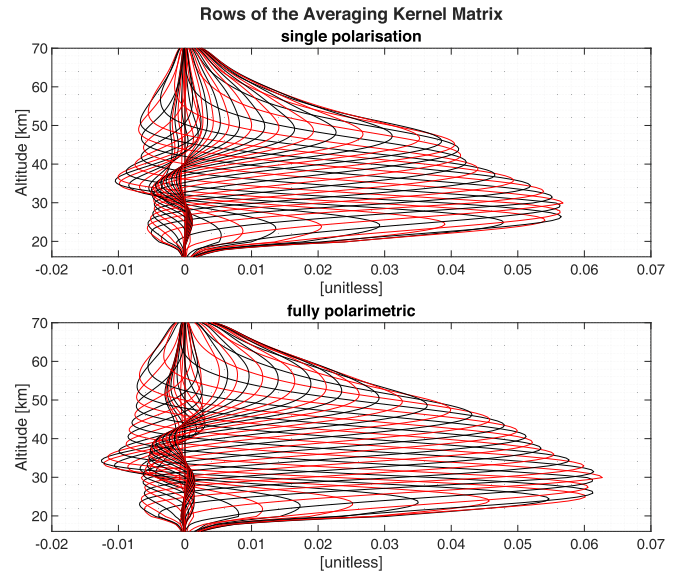

Fig. 4. Top: AVK for a retrieval with one simulated spectrum with total polarization. Bottom: AVK for a retrieval with two simulated spectra with RCP and LCP polarization.
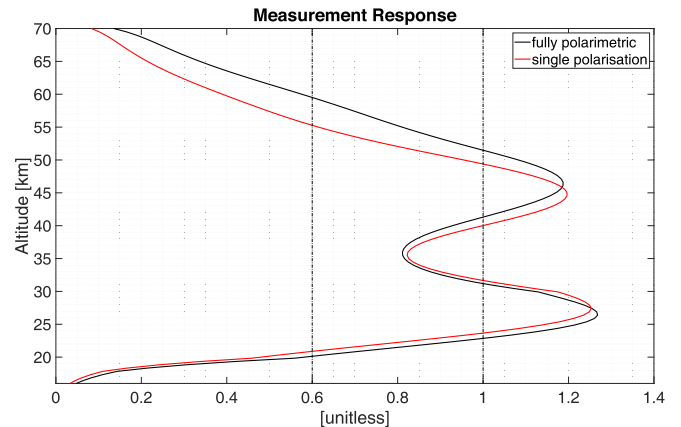

Fig. 5. Corresponding measurement response to the retrievals from Fig. 4. MR = 0.6 and MR = 1 are illustrated with the vertical dot-dashed lines.

polarization and observing geometry as in the observations with the line center at 53.067 GHz, an elevation of $60°$, and an azimuth of $90°$.

Above a certain altitude, this Zeeman broadening becomes larger than the pressure broadening. This limited the maximum height with significant measurement response of the retrieved temperature profiles of the first TEMPERA instrument to around 53 km.

V. Enhancing the Altitude Coverage of Temperature Retrievals by Polarimetric Decomposition

For observations in circular polarization, the Zeeman effect leads to a frequency shift of the line center with different signs for the left- and right-hand-circular polarization. Fig. 3 compares simulations of the line centers for LCP and RCP spectra with simulations in horizontal T_h and vertical T_v polarization. The observing geometry is the same as in Fig. 2. The LCP and RCP emission lines are narrower than the ones for linear polarization, and they will, thus, allow us to retrieve temperatures at higher altitudes. Furthermore, the frequency offset between

them allows us to derive information on the magnetic field strength (MFS). Figs. 4 and 5 illustrate the improvement that can be achieved by a simultaneous retrieval of the left- and right-circular spectra, compared to the previous state-of-the-art retrievals using a single linear polarization. The plots show the rows of the AVK (see Fig. 4) and the measurement response vector (see Fig. 5) from both retrievals that were performed with simulated emission spectra. The conditions of the simulation are summarized in Table I. Our simulations exhibit an increased MR combining LCP and RCP spectra in the retrieval while keeping the width of the AVK resulting in a similar vertical resolution at almost all the altitudes. Only between 27 and 46 km, the MR of the newer retrieval version shows slightly lower values. This dip originates from negative values of the AVK matrix at these altitudes, which occurs due to an overestimation of the apriori error.

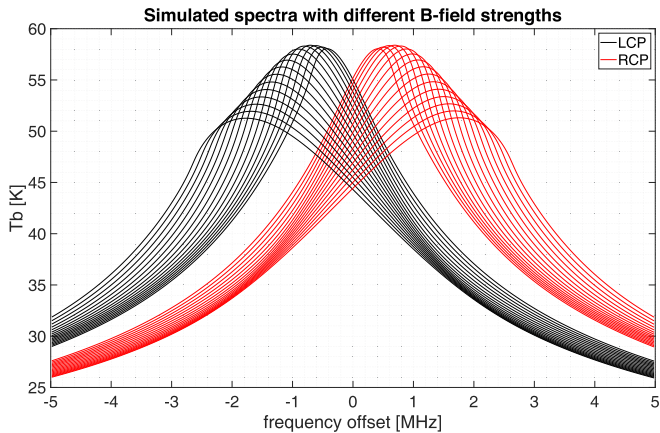|	
Center 1	52.542 GHz
Center 2	53.067 GHz
Bandwidth	2×100 MHz
Resolution	20 kHz
Noise	2 K
Latitude	7.45 E
Longitude	46.95 N
Azimuth	6°
Elevation	60°

Fig. 6.   Simulated spectra with the condition of Table I and different MFSs (see text). The line center is at 53.067 GHz. Radiative contribution from the troposphere was removed for this spectra.
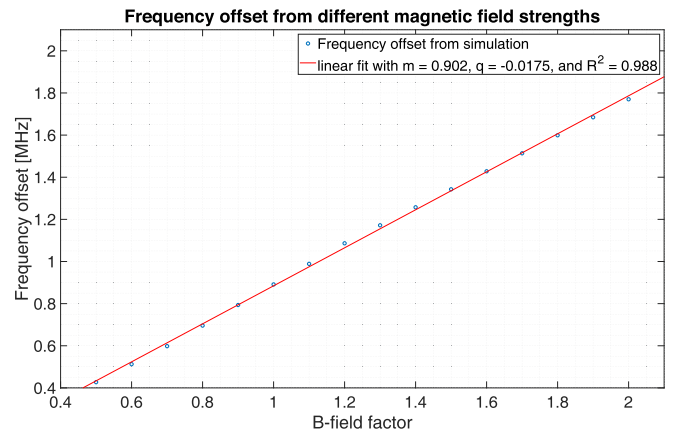

Fig. 7.   Frequency offset from the line center at 53.067 GHz due to different MFS.
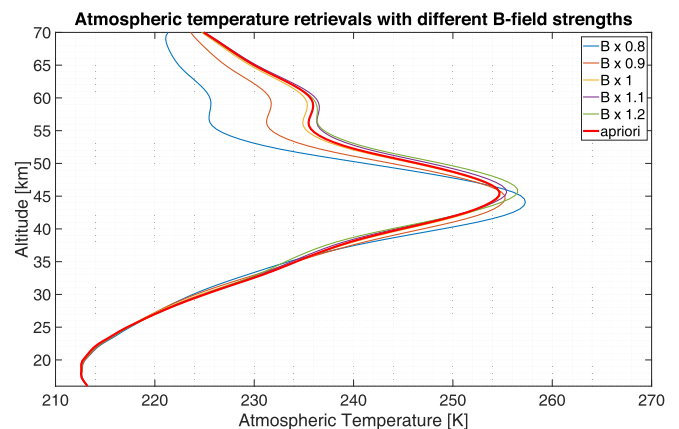
Fig. 8.   Atmospheric temperature from retrievals with different MFSs, retrieved with the same emission line.

VI. INFLUENCE OF THE MAGNETIC FIELD ON THE RETRIEVED PROFILE

The Zeeman-broadened lineshape depends on MFS, the polarization, and the angle between the line of sight of the instrument and the magnetic field lines. A study where linear polarized emission lines were measured for different azimuth angles, and hence with different angles between the line of sight and the magnetic field lines, is presented in [12]. In this section, the influence of the MFS is discussed. The Zeeman broadening gets stronger with increasing MFS. Fig. 6 shows simulated emission spectra at the line center of 53.067 GHz for LCP and RCP and different MFS. The reference magnetic field is the International Geometric Reference Field: 11th Generation, which is included in the ARTS. Contributions from the troposphere were removed in this case. The different MFSs were produced by multiplying the reference field with a factor between 0.5 and 2 with a step size of 0.1, yielding in total 16 different MFSs. The plot illustrates how the Zeeman broadening gets stronger with higher MFS. The line center offset is illustrated in Fig. 7. The relationship between this offset and the multiplication factor appears to be linear in this range of the magnetic field.

The influence of the MFS has to be considered in the retrieval because small deviations can produce large errors. If the MFS is underestimated, the measured emission line will be more Zeeman broadened as the forward model emission line. Therefore,

the pressure broadening (and with that the pressure as well) will be overestimated. This leads to an underestimation of the atmospheric temperature. That effect is illustrated in Fig. 8. It shows retrieved temperature profiles, where two emission spectra with LCP and RCP were simulated with the reference magnetic field and the conditions from Table I. From these spectra, temperature profiles were retrieved, using different MFSs by multiplying the reference magnetic field with factors between 0.8 and 1.2. Up to an altitude of about 35 km, the magnetic field has no significant influence on the retrieved profile. A cold bias occurs above 50 km in the profiles, which would result for an underestimated MFS. At the stratopause (45 km), a warm bias of around 2 K would be visible. We attribute this effect to decreased brightness temperatures of the line center due to the increased Zeeman broadening, which also results in a shift of a few megahertz of the line center for stronger MFS (see Fig. 6). Fig. 9 shows the difference between the retrieved profile and the apriori profile, which provides a better illustration of the resultant altitude-dependent biases and different MFSs. The retrieved temperature gets underestimated by around 5 K for the
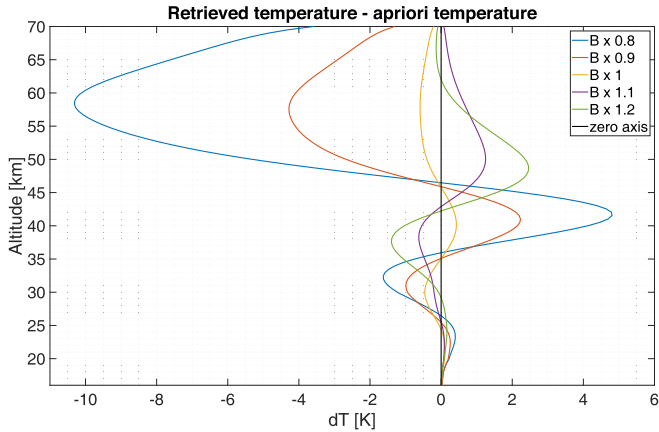
Fig. 9. Difference between retrieved temperature profiles with different MFSs and the apriori profile shows the expected behavior above 50 km.

factor 0.9 and 10 K for the factor 0.8, between an altitude of 50 and 60 km.

VII. INSTRUMENT DESCRIPTION

The novel TEMPERA-C instrument for atmospheric temperature sounding is based on our previous TEMPERA instrument, but it will perform simultaneous and fully polarimetric observations of two stratospheric emission lines. This will significantly improve the sensitivity and altitude range in the middle atmosphere compared to the current state of the art. The instrument uses an orthomode transducer (OMT) to split the two orthogonal polarization components, which are then processed by two identical receiver chains that share the same local oscillator (LO). The intermediate frequency bands are analyzed using a digital fast Fourier transform (FFT) spectrometer/correlator implemented on the "Universal Software Radio Peripheral" device (USRP X310).[1] A similar USRP with two UBX-160 daughterboards was first used for atmospheric Ozone measurements in [14]. For TEMPERA-C, we are using two TwinRX daughterboards. Each of them contains two coherent superheterodyne receivers. The two daughterboards are tuned to the line center of two different oxygen emission lines where they observe simultaneously the orthogonal polarizations. The baseband signals are digitized for each receiver with 200 MS/s and 14-bit resolution, and the on-board field-programmable gate array performs a real-time FFT analysis. The four complex spectra have a Nyquist bandwidth of 100 MHz and a resolution of 4096 channels each. These spectra are squared and accumulated independently to measure the total power in the two linear polarizations. In addition, they are correlated in real time, which allows us to derive the V-Stokes parameter and, hence, the left- and right-circular polarization spectra of the radiation. Similar digital spectrometers have been used previously for polarimetric observations in radio astronomy [15], but to our knowledge not for atmospheric remote sensing. Fig. 10 shows the schematic diagram of the TEMPERA-C polarimeter. The
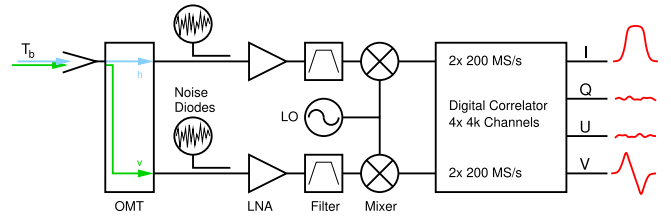
[1]USRP X310 with TwinRX Daughterboard from www.ettus.com

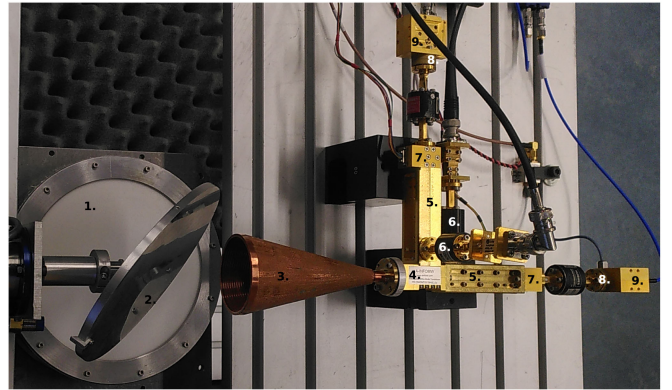Fig. 10. Schematic diagram of the TEMPERA-C polarimeter.

Fig. 11. Setup of the TEMPERA-C prototype with following components: *1) LN2 cold load; 2) rotating mirror; 3) feedhorn; 4) OMT; 5) coupler; 6) noise diodes; 7) low-noise amplifier (LNA); 8) bandpass filter; and 9) mixer.*

radiometric calibration of the instrument in operational use will be achieved by pointing the antenna at an ambient blackbody calibration target and injecting the signals of switchable noise diodes into the receivers through directional couplers. However, the prototype setup presented in this article was calibrated by switching the antenna between an ambient blackbody calibration target and a cold calibration target, consisting of a microwave absorber immersed in liquid nitrogen (LN2). Fig. 11 shows the setup of the initial TEMPERA-C prototype. The current prototype uses a simple Potter horn as feed and a flat rotating mirror for calibration. The final TEMPERA-C instrument will include a profiled corrugated feed, which is optimized to produce a symmetric ultra-Gaussian antenna pattern with low cross polarization, as well as a collimating quasi-optical network. More technical details are added in Table II.

VIII. POLARIMETRIC CALIBRATION

The digital correlator computes the square $|\langle E_h \rangle|^2, |\langle E_v \rangle|^2$ of both orthogonal polarized field components and its complex correlation $\langle E_h E_v^* \rangle$. In a first step, we assume an ideal and lossless receiver chain where the four output signals can be written in units of temperature as

$$A_h = |g_h \langle E_h \rangle|^2 + T_{Nh} \tag{14}$$

$$A_v = |g_v \langle E_v \rangle|^2 + T_{Nv} \tag{15}$$

$$A_U = 2\Re \{g_h g_v \langle E_h E_v^* \rangle\} \tag{16}$$

$$A_V = 2\Im \{g_h g_v \langle E_h E_v^* \rangle\}. \tag{17}$$

OMT	
Manufacturer	AINFO
Port-to-Port Isolation	<-43 dB
Insertion Loss	<0.5 dB
LNA	
Manufacturer	LNF
Gain	>33dB
Noise Figure	2.4 dB
Bandpass filter	
Manufacturer	In house
3-dB Corner Fr	50.8-54.2 GHz
Insertion loss	<0.6 dB
Mixer	
Type	VDI
DSB conversion Loss	<6 dB
DSB Noise Temperature	<700 K
Digital Correlator	
Manufacturer	Ettus
Type	USRP X310
Daughterboards	$2\times$ TwinRX
Bandwidth	4×100 MHz
Channels	4×4096
Resolution	24.4 kHz

Fig. 12. Spectra of atmospheric microwave radiation, measured with the TEMPERA-C prototype setup.

Here, g_h and g_v are the complex gains of the two receivers, and T_{Nh} and T_{Nv} are the corresponding receiver noise temperatures. With an analog correlator, the gain factors in (14)–(17) are not the same. With the digital spectrometer of TEMPERA-C, cross correlation is a completely numerical process, which allows the assumption that g_h and g_v in (14) and (15) are the same as in (16) and (17). The receiver noise is not included in the U and V components, because the radiometric noise of the two receiver chains is uncorrelated. It is common to use the Rayleigh–Jeans approximation; therefore, the relation between power and temperature units is linear. The gain, receiver noise, and brightness temperature are derived through a hot–cold load calibration, where the beam is switched alternately between the sky and two a known hot and cold blackbody source (see Fig. 11). The calibration equations for an ideal receiver are

$$T_h = A_h - T_{Nh} \tag{18}$$

$$T_v = A_v - T_{Nv} \tag{19}$$

$$T_V = A_V. \tag{20}$$

However, the breadboard receiver is far from ideal. Errors originate from multiple sources, which requires additional corrections, and thus, the simple approach from above is not suitable for practical implementation. Especially, the V-Stokes component is affected by even small errors, because its intensity is relatively low compared to the linear polarized components (see Fig. 12).
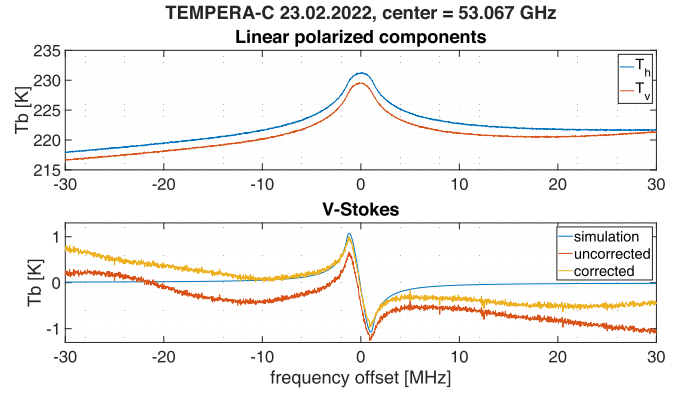
Possible error sources are the following.

1) The antenna pattern of the feedhorn is not the same for the two polarizations (asymmetry).
2) The OMT and feed do not ideally separate the polarization components (cross polarization).
3) Crosstalk between the two receiver chains after the OMT (crosstalk).

We assume that the main error source is cross polarization, which will be outlined in more detail in the following.

In a first step, we introduce frequency-dependent and complex cross-polarization terms c_h and c_v. The absolute value of c_h denotes the fraction of voltage leakage from the h-chain into the v-chain. The phase of c_h denotes the phase change of the leaked signal (and *vice versa* for c_v). With that, (14)–(17) can be rewritten in the following way:

$$A_h = |g_h (\langle E_h \rangle + c_v \langle E_v \rangle)|^2 + T_{Nh} \tag{21}$$

$$A_v = |g_v (\langle E_v \rangle + c_h \langle E_h \rangle)|^2 + T_{Nv} \tag{22}$$

$$A_U = 2\Re \{g_h g_v^* (\langle E_h \rangle + c_v \langle E_v \rangle) (\langle E_v \rangle + c_h \langle E_h \rangle)^*\} \tag{23}$$

$$A_V = 2\Im \{g_h g_v^* (\langle E_h \rangle + c_v \langle E_v \rangle) (\langle E_v \rangle + c_h \langle E_h \rangle)^*\}. \tag{24}$$

The goal is to derive c_h and c_v in order to correct the measurement by subtracting these terms. One approach to this problem is to use a fully polarimetric calibration target, consisting of hot and cold blackbodies, a polarizing wire grid, and a phase retardation plate [16]. In this article, we present a simpler alternative approach, which requires only unpolarized hot and cold blackbody targets. For these, we can assume that

$$\langle E_h E_v^* \rangle = 0 \quad \text{(black-body radiation)}. \tag{25}$$

Concerning the phases of the complex gains ϕ_h and ϕ_v, only their difference $\Delta\phi = \phi_h - \phi_v$ is of interest. Therefore, the following simplification can be made:

$$\phi_v = 0 \tag{26}$$

such that $\Delta\phi = \phi_h$, which was determined in a postprocess by a least-squares fit on the simulated spectrum. An additional simplification is to allow only for terms linear in c_h and c_v, which is justified by the assumption

$$|c_h c_v^*| \ll 1. \tag{27}$$

When the antenna beam is directed on the hot and cold target and with the assumptions (25) and (27), (23) and (24) become

$$A_U = 2\Re \left\{ g_h g_v^* \left(c_h^* |\langle E_h \rangle|^2 + c_v |\langle E_v \rangle|^2 \right) \right\} = 0 \quad (28)$$

$$A_V = 2\Im \left\{ g_h g_v^* \left(c_h^* |\langle E_h \rangle|^2 + c_v |\langle E_v \rangle|^2 \right) \right\} = 0. \quad (29)$$

With two targets, the above expression yields four equations to derive four unknowns contained in the two complex coefficients c_h and c_v. The complex gains g_h and g_v and the noise temperatures T_{Nh} and T_{Nv} can be derived beforehand by a hot/cold load calibration using (21) and (22).

Once the cross-polarization terms are known, the general correction term for the V-Stokes component reads as

$$C_V = 2\Im \left\{ g_h g_v^* \left(c_h^* |\langle E_h \rangle|^2 + c_v |\langle E_v \rangle|^2 \right) \right\}. \quad (30)$$

And the corrected V-Stokes component is simply the difference

$$T_V = A_V - C_V. \quad (31)$$

It has to be mentioned that the output signal consists of the partially cross-polarized field components with the receiver noise in addition $A_h/|g_h|^2$, $A_v/|g_v|^2$ [according to (23) and (24)], the pure fields $\langle E_h \rangle$ and $\langle E_v \rangle$ are not known. However, this appears to be of minor concern because considering the correction term [see (30)], cross-polarization terms cancels due to condition (27), and as mentioned above, the receiver noise is assumed to be uncorrelated. Therefore, it is reasonable to replace $\langle E_h \rangle$ and $\langle E_v \rangle$ with $A_h/|g_h|^2$ and $A_v/|g_v|^2$ in (23)–(30).

Fig. 12 shows the first polarimetric observations with the TEMPERA-C prototype after an integration time of about 12 h. The upper panel shows the brightness temperature around the 53.067-GHz emission line in the two orthogonal polarizations after a total power calibration with the hot and the cold target. We expect only a small difference between T_h and T_v at the line center, but not the observed offset on the line wings. Possible explanations for this calibration bias are the differences between the antenna pattern in the E- and H-planes of the feedhorn, the polarization dependence of the losses of the rotating calibration reflector, or a small nonlinearity of the receivers.

The lower panel of Fig. 12 shows the observed V-Stokes component of the correlator output with and without correction and compares it to the expected difference between the simulated LCP and RCP spectra. The observed signature close to the line center is very similar to the simulations in both the corrected and uncorrected spectra. The line wings, however, exhibit a slope of the baseline different from 0. This offset on the line wings is slightly improved by the corrections with (31), but a significant systematic bias remains. This means that apart from cross polarization, additional error sources affect the measurement. Fig. 13 illustrates the hot and cold load spectra of A_V and A_U before and after the correction. Condition (25) forces the corrected terms to zero. The measured LCP and RCP spectra after the correction are shown for the line center in Fig. 14.

IX. CONCLUSION

In this article, we illustrated that observations of oxygen emission lines between 52 and 54 GHz can be used for temperature sounding in the middle atmosphere and how the vertical range
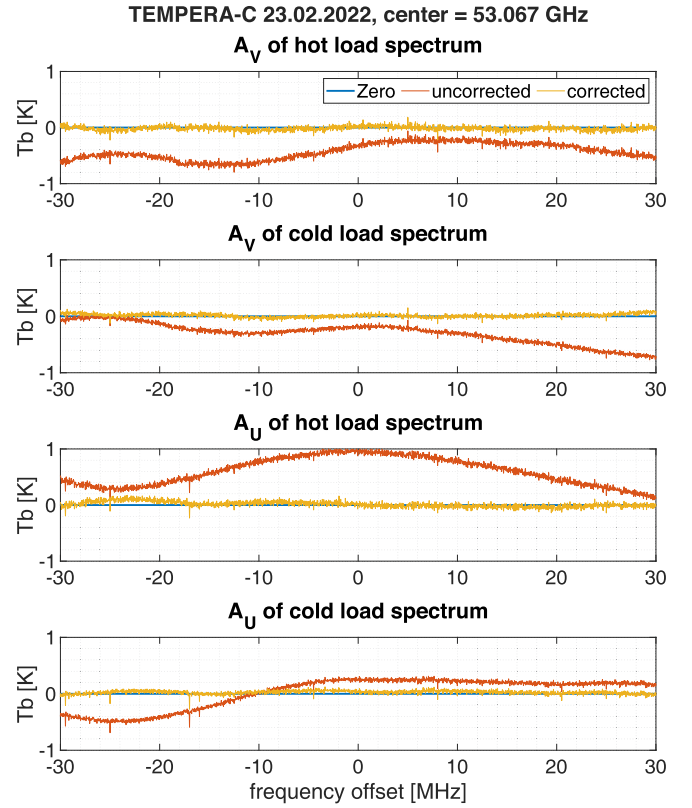

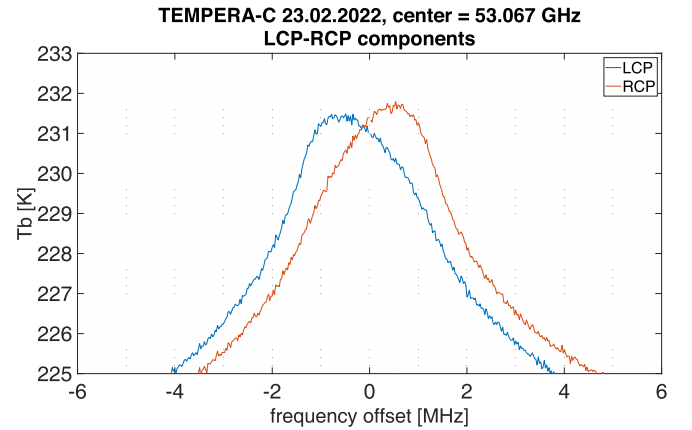Fig. 13. Illustration of hot and cold load spectra before and after correction.

Fig. 14. Illustration of LCP and RCP components estimated with corrected data.

of these retrievals is limited by the Zeeman effect. We further demonstrated by simulations that a simultaneous retrieval of LCP and RCP emission lines can improve the vertical range of the retrieval compared to the retrieval of a single emission line with linear polarization.

The increase in measurement response at 20–27 km can be explained by an increase of the signal-to-noise ratio by a factor of $\sqrt{2}$ by retrieving two instead of one spectra. The lower MR values between 27 and 46 km originate from a negative peak in the AVK at these altitudes, which is caused by an overestimation of the apriori error in this region. This small decrease, however,

does not affect the overall performance. In this study, we demonstrated that polarimetric observations of two oxygen emission lines and retrievals accounting for the Zeeman line splitting are beneficial to increase the MR at altitudes between 46 and 60 km. The improvement in the MR is about 12% (at 50 km) and 45% (at 60 km) higher than for the retrieval with single polarization. The effective upper altitude limit (altitudes with MR > 0.6) has increased from 55 km (with single polarization) to 59 km (fully polarimetric). The new TEMPERA-C instrument will provide fully polarimetric observations of the oxygen emission lines. Resolving the Zeeman splitting of the line center between the left- and right-circular polarization will extend the vertical range of the temperature retrievals into the lower mesosphere up to 60 km or above. First observations with a TEMPERA-C prototype receiver demonstrated the feasibility of the digital FFT spectrometer/correlator concept. Further work is needed to identify and correct additional error sources, such as a crosstalk between the receiver chains, to improve the polarimetric calibration of these observations.

REFERENCES

[1] O. Stähli, A. Murk, N. Kämpfer, C. Mätzler, and P. Eriksson, "Microwave radiometer to retrieve temperature profiles from the surface to the stratopause," *Atmos. Meas. Techn.*, vol. 6, no. 9, pp. 2477–2494, Sep. 2013.

[2] T. Rose, S. Crewell, U. Löhnert, and C. Simmmer, "A network suitable microwave radiometer for operational monitoring of the cloudy atmosphere," *Atmos. Res.*, vol. 75, no. 3, pp. 183–200, 2005, doi: 10.1016/j.atmosres.2004.12.005.

[3] H. H. Auman *et al.*, "AIRS/AMSU/HSB on the aqua mission: Design, science objectives, data products, and processing systems," *IEEE T. Geosci. Remote Sens.*, vol. 41, no. 2, 2003, doi: 10.3390/atmos11050490.

[4] X. Fuzhong *et al.* "Calibration of suomi national polar-orbiting partnership advanced technology microwave sounder," *J. Geophysical Res. Atmos.*, vol. 118, no. 19, pp. 11,187–11,200, 2013.

[5] A. A. Shvetsov *et al.*, "Ground-based sounding of the middle-atmosphere thermal structure in the frequency range 50-60 GHz," *Radiophys. Quantum Electron.*, vol. 54, nos. 8/9, pp. 569–576, 2012.

[6] K. Baumgarten and G. Stober, "On the evaluation of the phase relation between temperature and wind tides based on ground-based measurements and reanalysis data in the middle atmosphere," *Ann. Geophys.*, vol. 37, no. 4, pp. 581–602, 2019.

[7] F. Schranz, J. Hagen, G. Stober, K. Hocke, A. Murk, and N. Kämpfer, "Small-scale variability of stratospheric ozone during the sudden stratospheric warming 2018/2019 observed at Ny-ålesund, Svalbard," *Atmos. Chem. Phys.*, vol. 20, no. 18, pp. 10791–10806, 2020.

[8] W. Krochin, F. Navas-Guzmán, D. Kuhl, A. Murk, and G. Stober, "Continuous temperature soundings at the stratosphere and lower mesosphere with a ground-based radiometer considering the Zeeman effect," *Atmos. Meas. Techn.*, vol. 2021, pp. 1–28, 2021.

[9] S. A. Buehler, J. Mendrok, P. Eriksson, A. Perrin, R. Larsson, and O. Lemke, "ARTS, the Atmospheric Radiative Transfer Simulator—version 2.2, the planetary toolbox edition," *Geosci. Model Dev.*, vol. 11, no. 4, pp. 1537–1556, Apr. 2018.

[10] C. D. Rodgers, *Inverse Methods for Atmospheric Sounding: Theory and Practice*, Singapore: World Scientific, 2000.

[11] J. Randa *et al.*, "Recommended terminology for microwave radiometry," Nat. Inst. Standards Technol., Gaithersburg, MD, USA, Tech. Note TN1551, 2008.

[12] F. Navas-Guzmán, N. Kämpfer, A. Murk, R. Larsson, S. A. Buehler, and P. Eriksson, "Zeeman effect in atmospheric O_2 measured by ground-based microwave radiometry," *Atmos. Meas. Techn.*, vol. 8, no. 4, pp. 1863–1874, Apr. 2015.

[13] R. Larsson, B. Lankhaar, and P. Eriksson, "Updated Zeeman effect splitting coefficients for molecular oxygen in planetary applications," *J. Quant. Spectrosc. Radiat. Transf.*, vol. 224, pp. 431–438, 2019.

[14] J. Hagen, A. Luder, A. Murk, and N. Kämpfer, "Frequency-agile FFT spectrometer for microwave remote sensing applications," *Atmosphere*, vol. 11, no. 5, 2020, Art. no. 490.

[15] A. Alvear *et al.*, "FPGA-based digital signal processing for the next generation radio astronomy instruments: Ultra-pure sideband separation and polarization detection," in *Proc. SPIE*, vol. 9914, pp. 332–345, 2016.

[16] J. Lahtinen, A. J. Gasiewski, M. Klein, and I. S. Corbella, "A calibration method for fully polarimetric microwave radiometers," *IEEE Trans. Geosci. Remote Sens.*, vol. 41, no. 3, pp. 588–602, Mar. 2003.

Witali Krochin received the bachelor.s degree in physics and the master's degree in theoretical physics, in 2017 and 2020, respectively, from the University of Bern, Bern, Switzerland, where he is currently working toward the Ph.D. degree in microwave physics with the Institute of Applied Physics.

Gunter Stober received the Diploma in physics and the Ph.D. degree in meteor physics from the University of Leipzig, Leipzig, Germany, in 2006 and 2009, respectively, and the Habilitation in microwave physics from the University of Bern, Bern, Switzerland, in 2020.

He is currently a Lecturer of meteor physics, microwave physics, and atmospheric dynamics with the University Bern. Since 2022, he has been the Head of the Atmospheric Processes and Radiometry Group.

Axel Murk received the master's degree from the Technical University of Munich, Munich, Germany, in 1995, and the Ph.D. degree from the University of Bern, Bern, Switzerland, in 1999, both in physics.

Since 2018, he has been the Head of the Microwave Physics Division.